Published in final edited form as:
J Struct Biol. 2010 August ; 171(2): 125–132. doi:10.1016/j.jsb.2010.04.005.

Ion-abrasion scanning electron microscopy reveals distorted liver mitochondrial morphology in murine methylmalonic acidemia

Gavin E. Murphy[1], **Bradley C. Lowekamp**[2], **Patricia M. Zerfas**[3], **Randy J. Chandler**[4,5,1], **Charles P. Venditti**[5], and **Sriram Subramaniam**[1,*]

[1] Laboratory of Cell Biology, Center for Cancer Research, National Cancer Institute, NIH, Bethesda, MD 20892 USA

[2] Office of High Performance Computing and Communications, National Library of Medicine, NIH, Bethesda, MD 20814 USA

[3] Division of Veterinary Resources, Office of Research Services, NIH, Bethesda, MD 20814 USA

[4] Institute for Biomedical Sciences, The George Washington University, Washington, DC 20037 USA

[5] Organic Acid Research Section, Genetics and Molecular Biology Branch, National Human Genome Research Institute, NIH, Bethesda, MD 20814 USA

Abstract

Methylmalonic acidemia is a lethal inborn error of metabolism that causes mitochondrial impairment, multi-organ dysfunction and a shortened lifespan. Previous transmission electron microscope studies of thin sections from normal ($Mut^{+/+}$) and diseased ($Mut^{-/-}$) tissue found that the mitochondria appear to occupy a progressively larger volume of mutant cells with age, becoming megamitochondria. To assess changes in shape and volume of mitochondria resulting from the mutation, we carried out ion-abrasion–scanning electron microscopy (IA–SEM), a method for 3D imaging that involves the iterative use of a focused gallium ion beam to abrade the surface of the specimen, and a scanning electron beam to image the newly exposed surface. Using IA–SEM, we show that mitochondria are more convoluted and have a broader distribution of sizes in the mutant tissue. Compared to normal cells, mitochondria from mutant cells have a larger surface-area-to-volume ratio, which can be attributed to their convoluted shape and not to their elongation or reduced volume. The 3D imaging approach and image analysis described here could therefore be useful as a diagnostic tool for the evaluation of disease progression in aberrant cells at resolutions higher than that currently achieved using confocal light microscopy.

Keywords

Scanning Electron Microscopy; Focused Ion Beam; Ion Abrasion; Mitochondria; Methylmalonic Acidemia; Diagnostic Imaging

[*]Corresponding author. Phone +1 301 594 2062. Fax +1 301 480 3834. ss1@nih.gov.

1. Introduction

Methylmalonic acidemia (MMA) is an autosomal recessive inborn error of metabolism caused by an inability of the 5′deoxycobalamin-dependent enzyme methylmalonyl-CoA mutase (MUT) to convert methylmalonyl-CoA to succinyl-CoA [1]. Patients suffer frequent metabolic decompensation, which causes an accumulation of methylmalonic acid in blood and tissues [1]. Multiple organs in the patients are compromised including the liver, kidney, pancreas and basal ganglia [2]. Patients have a shortened lifespan and require liver or kidney transplantation for survival [3]. Previous studies using (diseased) tissues from *Mut* $^{-/-}$ mice and the native liver from a patient with methylmalonic acidemia have demonstrated that morphological changes are present in mitochondria in the hepatocytes, proximal tubular renal epithelium and the pancreas, but not in other high energy tissues, such as the heart or skeletal muscle [4].

Analysis of the ultrastructural origins of the diseased phenotype using 2D transmission electron microscope (TEM) imaging revealed systemic, widespread mitochondrial enlargement into “megamitochondria” as the disease progressed in older mice, though the amount of liver mitochondria in the *Mut* $^{-/-}$ tissue was similar, as measured by mitochondrial DNA levels [5; 4]. The functional consequences of such changes in liver mitochondria manifest as widespread respiratory chain dysfunction and diminished reducing ability [4]. Lipid bodies also appeared to proliferate and enlarge in *Mut* $^{-/-}$ mouse liver [4]. These conclusions were derived from the inspection of many 2D images. A three-dimensional reconstruction of tissue would allow a quantitative comparison of mitochondrial and lipid droplet morphology and elucidate the early steps, and possible mechanism, of megamitochondria formation in selected cell types in this disorder. To extend the insights derived from 2D TEM imaging, we have used ion-abrasion–scanning electron microscopy (IA–SEM) [6–13], a newly emerging imaging technology, to compare the 3D architectures of mitochondria from normal and mutant tissue. In this automated approach for 3D imaging, a gallium ion beam iteratively abrades material off the surface of a macroscopic specimen such as plastic-embedded cells or tissues (typically in steps of ~15 nm to 50 nm), and an electron beam generates an image of the newly revealed face to produce a stack of 2D images.

The use of IA–SEM helps fill an important gap in imaging between light microscopy (~1 μm resolution) and higher resolution techniques such as transmission electron microscopy (~1 nm resolution or better) by providing 3D maps of whole organelles, cells and tissues at an intermediate resolution (~20–40 nm). Thus, while light microscopic methods now allow imaging beyond the diffraction limit, the visualization is limited to fluorescently tagged species at resolutions in the very best cases of ~15–100 nm in the imaging plane and ~100 nm along the optical axis [14]. With TEM, imaging is typically limited to sections with thicknesses in the range of ~50 to ~500 nm. The structural information in each section can be obtained either as a 2D projection image, or as a 3D volume using electron tomography. Thus, to reconstruct 3D images of large mammalian cells whose thicknesses typically exceed 10 microns, samples must be sectioned into a series of thin sections, and imaged in such a way that the 2D or 3D images from each section can be aligned in a stack to obtain the 3D image of the cell. This is a feasible approach, but can be time-consuming and tedious in practice, and subject to artifacts arising from loss of material between successive sections, and missing wedge distortion, when serial tomographic reconstructions are employed[15]. Alternative approaches such as X-ray tomography are at early stages of development, but remain at significantly lower resolutions that what can be achieved by either IA–SEM or TEM [16].

Here, we have used IA–SEM to carry out a quantitative analysis of comparative mitochondrial morphologies obtained from the liver of 4-day-old, healthy, control and 4-day-old, diseased, *Mut* $^{-/-}$ mice. Under these conditions, hepatocytes in the diseased mice are captured at a stage when structural changes to the mitochondria begin to appear, but before completion of

conversion to megamitochondria. The technical focus of this work is to develop and evaluate quantitative tools to analyze 3D volumetric data in IA–SEM as they relate to describing subcellular changes in diseased cells and tissues.

2. Methods

2.1 Western blotting

Animal studies were reviewed and approved by the National Human Genome Research Institute Animal User Committee. The mutase-deficient, diseased mice, called *Mut* $^{-/-}$, were produced as described [4]. Tissue samples were homogenized with a 2-ml Tenbroeck tissue grinder (Wheaton, Millville, NJ) in T-PER (Pierce Biotechnology, Rockford, IL) tissue protein extraction buffer in the presence of Halt (Pierce Biotechnology) protease inhibitor cocktail. Sixty micrograms of clarified extract were used in Western analysis and probed with affinity-purified, rabbit polyclonal antisera raised against the murine methylmalonyl-CoA mutase enzyme [17]. Complex III Core II was used as a loading control and was also detected by immunoblotting [mouse monoclonal anti-OxPhos Complex III (ubiquinol-cytochrome c oxidoreductase) Core II antibody, Invitrogen SKU# A-11143]. The anti-mutase antibody was used at a dilution of 1:750 and the anti-Complex III Core II antibody was used at a dilution of 1:2000. Horseradish peroxidase (HRP)-conjugated antirabbit IgG (NA934; GE Healthcare Life Sciences, Piscataway, NJ) or rabbit antigoat IgG (sc-2768; Santa Cruz Biotechnology) was used as the secondary antibody and was visualized with chemiluminescence detection (Pierce Biotechnology).

2.2 Preparation of plastic-embedded liver tissue

Fresh liver tissue from a control and from a *Mut* $^{-/-}$ littermate were obtained on their fourth day of life and fixed in 2 % glutaraldehyde in 0.1 M cacodylate buffer (pH 7.4) overnight at 4° C. The tissues were washed with cacodylate buffer and postfixed with 2% OsO4 for two hours. The tissue was washed again with 0.1 M cacodylate buffer, serially dehydrated in ethanol and embedded in EMBed 812 resin (Electron Microscopy Sciences, Hatfield, PA, USA).

2.3 Tomography procedures

Thin sections, ~70 –80 nm thick, were obtained by utilizing the Leica ultracut-UCT ultramicrotome (Leica, Deerfield, IL, USA) and placed onto 200 mesh copper grids. 10 nm gold was applied to the grids and excess was washed off. The grids were loaded into a Gatan High-Tilt holder and placed into a FEI Tecnai T12 electron microscope operated at 120 kV with a LaB_6 filament. Images were collected on a Gatan 4k CCD with a binning factor of 2. Tomograms were acquired automatically using Inspect3D (FEI) with a nominal magnification of 21,000, a sampling of 10.8 Å/pixel, a dose of ~1000 $e^-/Å^2$, an underfocus of 2.5 μm, tilt extrema of 66° or 70°, and a tilt increment of 2°. Single-axis tilt series were aligned and tomograms generated using IMOD [18].

2.4 Ion-abrasion–SEM procedures

The resin-embedded specimen block was trimmed to a 1 mm^2 pyramidal face with a razor blade. Ultrathin sections were prepared using a microtome and surveyed in a TEM to identify regions suitable for imaging. The top of the block was then removed and attached to a SEM stub using silver paint. The stub and specimen were then sputter-coated with gold to reduce specimen charging. The specimen was loaded into a Nova 200 Nanolab DualBeam™ SEM/FIB (FEI, Hillsdale, OR). A ~0.5 μm thick layer of platinum was deposited on a region of interest using a gas injector system and the ion beam was set to 30 kV and 0.5 nA. In front of the region, a trench was created using the ion beam at a 7 nA current. The sample was again sputter-coated to ensure conductance and reduce charging on the exposed surface. The exposed

face was polished using the ion beam at 5 nA. Conditions used for data collection were 3kV for the electron beam at a 0.27 nA current, an extraction voltage of −50 V for the Everhart-Thornley detector, and an effective magnification of 10383× (3 nm/pixel), corresponding to a horizontal field width of 12.3 μm (4096×3036 pixels). 2D image stacks were collected using the 'slice-and-view' imaging module (FEI) with a nominal sectioning thickness of 40 nm.

2.5 Image processing and analysis

SEM image stacks were iteratively and automatically aligned using the IMOD tiltxcorr program and a customized script. The contrast was inverted solely for purposes of visualization to facilitate comparison to TEM images, and denoised using anisotropic diffusion based methods implemented in IMOD. SEM images were 12.3 long and 10.6 μm wide. After images were aligned, the volume was trimmed to create a volume that contained only data, not background grey values, with dimensions of ~12 × 8 × 4 μm in each case. To produce Fig. 2, the volume was non-isotropically binned by 4 to produce a 12 nm pixel size and the z dimension of 40 nm was interpolated to 12 nm. The mitochondria and lipid bodies were segmented manually with the Amira brush tool on the original stack (Amira, Visage Imaging, Andover, MA). The individual mitochondrial and lipid body volumes and the mitochondrial surface area were measured using Amira. To make the comparisons shown in panels B, C, E and F more meaningful, the numbers of mitochondria in control and Mut $^{-/-}$ cells were scaled to the 3D volumes of the respective stacks (see legend to Figure 3). The Gaussian curvature for each mitochondrion was calculated using the Segmentation and Registration Toolkit from Insight (www.itk.org), as follows. The surfaces were extracted from the segmentation and resampled into isotropic 21.9 nm voxels. The morphological closing of the volume was performed using a binary structured element with a radius of 4 voxels. 100 iterations of the level-set–based, curvature-flow smoothing filter were then applied to further remove small features with high curvature [19]. The Gaussian curvature was computed for the isosurfaces contained in the volumes using a recursive derivative of Gaussian filters with a sigma of 40 nm, a method previously described [20]. The curvature values were then extracted at each voxel on the smoothed contour representing the mitochondria.

3. Results

To ascertain whether there were gross changes in mitochondrial mass between the *Mut* $^{-/-}$ and control samples, *Mut* and mitochondrial enzyme levels were assessed by Western blotting (Figure 1A). These experiments show that although the mutase-deficient mice lacked a detectable amount of mutase, as expected, the amount of a marker for mitochondrial mass, i.e., oxidative phosphorylation enzyme Q-cytochrome c oxidoreductase (complex III) core II, was similar (p=0.11). This result, in combination with mitochondrial DNA similarities[4], shows that bulk mitochondrial protein and DNA mass are similar in the *Mut* $^{-/-}$ and control tissues, laying the foundation for the more quantitative comparative analyses we carried out.

Initially, we used electron tomography of thick sections to get an initial impression of morphological differences between control (Figures 1B–D) and *Mut* $^{-/-}$ (Figures 1E–G) mitochondria. In both cases, the general appearance of mitochondrial cross-sections and cristae is comparable, indicating that differences if any, would only be apparent in 3D images of a larger volume. In contrast, IA–SEM imaging of the tissue specimens revealed measurable differences. Inspection of single SEM slices through the stack suggested that mitochondria occupy a greater region of the sampled *Mut* $^{-/-}$ cells than of the sampled control cells (Figure 2). This difference is further underscored in the segmented representation of 3D images of the cells (Figure 3), which reveal higher mitochondrial density and greater contortion in the *Mut* $^{-/-}$ tissue (see also Supplementary Movies 1–4). Because the reconstructions are of a portion of liver tissue cells, some of the mitochondria run off the edges and are imaged only

partially. These partially represented control and *Mut* $^{-/-}$ mitochondria are respectively colored aqua and pink in Figure 3, while the whole mitochondria are respectively colored blue and red. To eliminate any bias from the use of partial mitochondria, the conclusions we present here are derived only from analysis of whole mitochondria. We note, however, that because of the large numbers of mitochondria included in our analysis, the same trends and variations were also observed when only the partial mitochondria were included in the analysis, or when both whole and partial mitochondria were considered together.

Mitochondria in the reconstructed *Mut* $^{-/-}$ liver tissue volume are more numerous and, in total sum, more voluminous. Based on consideration of 80 whole and 113 partial mitochondria in the *Mut* $^{-/-}$ tissue, and 40 whole and 57 partial mitochondria in the control tissue, we find that the relative volume occupied by mitochondria is ~68% higher in *Mut* $^{-/-}$ tissue (23% versus 14% of the reconstructed volume occupied by mitochondria, for *Mut* $^{-/-}$ and control tissue, respectively), as measured by the segmentation of volumes corresponding to mitochondria. As evident in single slices, lipid bodies are present in both control and *Mut* $^{-/-}$ tissue, but in contrast to the difference in mitochondrial volumes, differences in lipid are less than 5% in volume (20% versus 18% for control and *Mut* $^{-/-}$ tissue, respectively).

The *Mut* $^{-/-}$ mitochondria are more numerous and occupy a larger total volume and also display greater variation in volume and in surface area (Table 1). The volume and surface area distributions of both control and *Mut* $^{-/-}$ mitochondria are non-normal and have a positive skew. Because the distributions are not normal, a two-tailed Mann-Whitney test was used to compare the median mitochondrial volumes and surface areas, and we established that the distributions are not statistically different (Figure 4). The disproportionately higher surface area of mitochondria in *Mut* $^{-/-}$ tissue (cf. Figures 4C and 4F) suggested that they may be more convoluted in shape, and we assessed this in further detail by comparing median surface area to volume ratios.

As summarized in Table 2, the mean surface-area-to-volume ratios of *Mut* $^{-/-}$ mitochondria are 23% higher than in control mitochondria, a significant difference according to a two-tailed Mann-Whitney test (Figure 5A). The increased surface-area-to-volume ratio in *Mut* $^{-/-}$ mitochondria is not due to the numerous, small, *Mut* $^{-/-}$ mitochondria, which might have skewed the results. To establish this point quantitatively, we show that the surface area relative to volume of the control mitochondria lie along a line $\text{SurfaceArea} = m * \text{Volume}^{2/3}$, with $m = 5.7$ ($R^2 = 0.996$) (Figure 5B). In contrast, the *Mut* $^{-/-}$ mitochondria fall into two groups. Most of the *Mut* $^{-/-}$ mitochondria lie along the line fit to the control mitochondrial ratios, but 32% of the *Mut* $^{-/-}$ mitochondria (hereafter called abnormal) have enlarged surface areas throughout the range of volumes. A line was fit for all the *Mut* $^{-/-}$ points with $m = 7.4$ ($R^2 = 0.94$).

An interesting result that emerges from the 3D visualization is that the abnormal *Mut* $^{-/-}$ mitochondria are clearly more convoluted and display greater curvature variation across the surface. To compare the geometric deformities of *Mut* $^{-/-}$ mitochondria to the mostly spheroidal control ones, the Gaussian curvature along the whole surface of each mitochondrion was measured. Gaussian curvature is positive for concave or convex regions and negative for hyperbolic regions. A spheroid only has positive curvature. Upon visual inspection of the surfaces, concave regions appeared to be relatively rare while negative curvature seemed more common in *Mut* $^{-/-}$ surfaces. A metric was therefore chosen to differentiate the two types of surfaces. The curvature at each point was categorized and the percent positive Gaussian curvature (PPGC) was output. The percentage of the curvature that was positive, i.e., that displayed convex or concave curvature, was tabulated in Table 2 and displayed as a histogram in Fig. 6A. The median value of the PPGC was 91.2% and 87.4% for control and *Mut* $^{-/-}$ mitochondria, respectively. The median values were significantly different according to a two-tailed Mann-Whitney test. Fig. 6A shows that the *Mut* $^{-/-}$ mitochondrial curvature appears to

be bimodal, with most *Mut* $^{-/-}$ mitochondria being similar to control ones, yet many (32%) having more hyperbolic curvature. Those mitochondria with a PPGC less than 75% are defined as abnormal, because the lowest PPGC seen in control mitochondria is 75% in this study. In order to view the general shape of normal and abnormal mitochondria, Figure 6B shows *Mut* $^{-/-}$ tissue with abnormal, whole, mitochondria colored red and normal, whole mitochondria colored pink. Figure 5B and Figure 6A can be compared, for instance, in that the twelve *Mut* $^{-/-}$ mitochondria with the largest surface area in relation to volume (the points in Fig. 5B that lie along the upper part of the *Mut* $^{-/-}$ fit) also all had high amounts of hyperbolic curvature, with their PPGC less than 69%. Thus, *Mut* $^{-/-}$ mitochondria with unusually high surface areas at any given volume also have more hyperbolic curvature. This is illustrated in Figures 6C–I using color-coding to reflect curvature. While control mitochondria (Figures 6C–E) and normal *Mut* $^{-/-}$ mitochondria are mostly shaped like oblate spheroids with convex Gaussian curvature, abnormal *Mut* $^{-/-}$ mitochondria (Figures 6F–I) are largely distorted, with substantially more hyperbolic curvature. Control mitochondria in Figures 6C–E have a PPGC of 77%, 96% and 100%, respectively, while abnormal *Mut* $^{-/-}$ mitochondria in Figures 6F–I have a PPGC of 55%, 58%, 66% and 70%, respectively. The volume of the normal, whole *Mut* $^{-/-}$ mitochondria comprise only ~ 45% of the total whole mitochondrial population, and the relative proportion of the sample volume occupied by these “normal” mitochondria is less (only ~70%) than the relative proportion occupied by “normal” mitochondria in the control tissue sample. This is because the average size of the normal, whole, *Mut* $^{-/-}$ mitochondria is smaller (only ~65%) than whole control mitochondria.

4. Discussion

Our results show that though individual mitochondria from 4-day-old, *Mut* $^{-/-}$ mouse liver had similar median volumes, surface areas and matrix marker protein mass as compared to control tissue, they are more numerous and therefore occupy a greater proportion of cellular volume and displayed a broader distribution of sizes. The similar amounts of the mitochondrial matrix marker, together with the increased volume, suggest that protein mass does not scale with volume, possibly because the volume increase originates from changes in concentration and amount of metabolic intermediates, and not from a proportional enlargement of mitochondria. 32% of the mitochondria possessed a higher surface-area-to-volume ratio and more hyperbolic curvature than control mitochondria and accounted for 55% of the mitochondrial volume fraction. Examination of individual volumes showed that mitochondria with unusually high surface area at any volume also had more hyperbolic curvature. In addition, no excessive lipid accumulation was found in the 4-day-old, *Mut* $^{-/-}$ mouse liver compared to control tissue.

An increase in mitochondrial surface area does not imply an increase in hyperbolic curvature – for example, a mitochondrion with a tubular shape (i.e. a lengthened ellipsoid) could have a greater surface area than an ellipsoidal one, but it would not have any hyperbolic curvature. On the other hand, if the tube were branched, it would have hyperbolic curvature at the branch points. One possible origin of the observed increase in both hyperbolic curvature and surface area (with respect to volume) could be an increase in mitochondrial fusion or a failure to complete mitochondrial fission, because the plane of contact would have hyperbolic curvature. Megamitochondria are believed to form not by simple osmotic swelling, but perhaps by increased fusion, decreased fission or hypertrophy [5]. Mitochondria normally undergo periodic fusion and fission. Mitochondria in COS7 and INS1 cells undergo fusion every ~5–20 minutes, followed by fission ~100 seconds later [21]. The presence of large, hyperbolic *Mut* $^{-/-}$ mitochondria in our study, however, is accompanied by an increase in small mitochondria, which one might speculate is the product of increased fission. An explanation for the increase in small and large mitochondria might therefore be due to a perturbation of normal mitochondrial fission and fusion behavior.

The work we have presented here demonstrates the use of IA–SEM to provide quantitative assessments of 3D morphological differences of subcellular organelles in tissue at nanoscale resolution. This type of analysis could thus potentially form the basis of a diagnostic tool to evaluate disease progression using metrics that report on quantitative differences between control and diseased cells at resolutions substantially higher than that achieved using confocal light microscopy.

Supplementary Material

Refer to Web version on PubMed Central for supplementary material.

Acknowledgments

This research was supported by the Center for Cancer Research, which is the Intramural Research Program of the National Cancer Institute, NIH.

References

1. Fenton, WA.; Gravel, RA.; Rosenblatt, DS. Disorders of Propionate and Methylmalonate Metabolism. In: Scriver, CR., et al., editors. The Metabolic and Molecular Bases for Inhertited Disease. McGraw-Hill, Inc; New York: 2001. p. 2165-2192.
2. Horster F, Baumgartner MR, Viardot C, Suormala T, Burgard P, Fowler B, Hoffmann GF, Garbade SF, Kolker S, Baumgartner ER. Long-term outcome in methylmalonic acidurias is influenced by the underlying defect (mut0, mut-, cblA, cblB). Pediatr Res 2007;62:225–30. [PubMed: 17597648]
3. Leonard JV, Walter JH, McKiernan PJ. The management of organic acidaemias: the role of transplantation. J Inherit Metab Dis 2001;24:309–11. [PubMed: 11405351]
4. Chandler RJ, Zerfas PM, Shanske S, Sloan J, Hoffmann V, DiMauro S, Venditti CP. Mitochondrial dysfunction in mut methylmalonic acidemia. FASEB J 2009;23:1252–61. [PubMed: 19088183]
5. Wakabayashi T. Megamitochondria formation - physiology and pathology. J Cell Mol Med 2002;6:497–538. [PubMed: 12611638]
6. Subramaniam S. Bridging the imaging gap: visualizing subcellular architecture with electron tomography. Curr Opin Microbiol 2005;8:316–22. [PubMed: 15939356]
7. Heymann JA, Hayles M, Gestmann I, Giannuzzi LA, Lich B, Subramaniam S. Site-specific 3D imaging of cells and tissues with a dual beam microscope. J Struct Biol 2006;155:63–73. [PubMed: 16713294]
8. Drobne D, Milani M, Leser V, Tatti F, Zrimec A, Znidarsic N, Kostanjsek R, Strus J. Imaging of intracellular spherical lamellar structures and tissue gross morphology by a focused ion beam/scanning electron microscope (FIB/SEM). Ultramicroscopy 2008;108:663–70. [PubMed: 18068303]
9. Knott G, Marchman H, Wall D, Lich B. Serial section scanning electron microscopy of adult brain tissue using focused ion beam milling. J Neurosci 2008;28:2959–64. [PubMed: 18353998]
10. Bennett AE, Narayan K, Shi D, Hartnell LM, Gousset K, He H, Lowekamp BC, Yoo TS, Bliss D, Freed EO, Subramaniam S. Ion-abrasion scanning electron microscopy reveals surface-connected tubular conduits in HIV-infected macrophages. PLoS Pathog 2009;5:e1000591. [PubMed: 19779568]
11. De Winter DA, Schneijdenberg CT, Lebbink MN, Lich B, Verkleij AJ, Drury MR, Humbel BM. Tomography of insulating biological and geological materials using focused ion beam (FIB) sectioning and low-kV BSE imaging. J Microsc 2009;233:372–83. [PubMed: 19250458]
12. Heymann JA, Shi D, Kim S, Bliss D, Milne JL, Subramaniam S. 3D imaging of mammalian cells with ion-abrasion scanning electron microscopy. J Struct Biol 2009;166:1–7. [PubMed: 19116171]
13. Hildebrand M, Kim S, Shi D, Scott K, Subramaniam S. 3D imaging of diatoms with ion-abrasion scanning electron microscopy. J Struct Biol 2009;166:316–28. [PubMed: 19269330]
14. Huang B, Jones SA, Brandenburg B, Zhuang X. Whole-cell 3D STORM reveals interactions between cellular structures with nanometer-scale resolution. Nat Methods 2008;5:1047–52. [PubMed: 19029906]

15. Noske AB, Costin AJ, Morgan GP, Marsh BJ. Expedited approaches to whole cell electron tomography and organelle mark-up in situ in high-pressure frozen pancreatic islets. J Struct Biol 2008;161:298–313. [PubMed: 18069000]

16. Parkinson DY, McDermott G, Etkin LD, Le Gros MA, Larabell CA. Quantitative 3-D imaging of eukaryotic cells using soft X-ray tomography. J Struct Biol 2008;162:380–6. [PubMed: 18387313]

17. Chandler RJ, Tsai MS, Dorko K, Sloan J, Korson M, Freeman R, Strom S, Venditti CP. Adenoviral-mediated correction of methylmalonyl-CoA mutase deficiency in murine fibroblasts and human hepatocytes. BMC Med Genet 2007;8:24. [PubMed: 17470278]

18. Kremer JR, Mastronarde DN, McIntosh JR. Computer visualization of three-dimensional image data using IMOD. J Struct Biol 1996;116:71–6. [PubMed: 8742726]

19. Sethian, JA. Level set methods and fast marching methods. Cambridge University Press; 1999. Image Enhancement and Noise Removal; p. 118

20. Kindlmann, G.; Whitaker, R.; Tasdizen, T.; Moller, T. Curvature-Based Transfer Functions for Direct Volume Rendering: Methods and Applications. Proceedings of the 14th IEEE Visualization 2003 (VIS'03); IEEE Computer Society; 2003.

21. Twig G, Elorza A, Molina AJ, Mohamed H, Wikstrom JD, Walzer G, Stiles L, Haigh SE, Katz S, Las G, Alroy J, Wu M, Py BF, Yuan J, Deeney JT, Corkey BE, Shirihai OS. Fission and selective fusion govern mitochondrial segregation and elimination by autophagy. EMBO J 2008;27:433–46. [PubMed: 18200046]

Appendix A. Supplementary Material

Supplementary data associated with this article includes Supp. Movie 1 and Supp. Movie 2, which are orthoslice movies of the control and *Mut* $^{-/-}$ volumes, respectively, and Supp. Movie 3 and Supp. Movie 4, which are movies of the segmented mitochondria from the control and *Mut* $^{-/-}$ volumes, respectively.

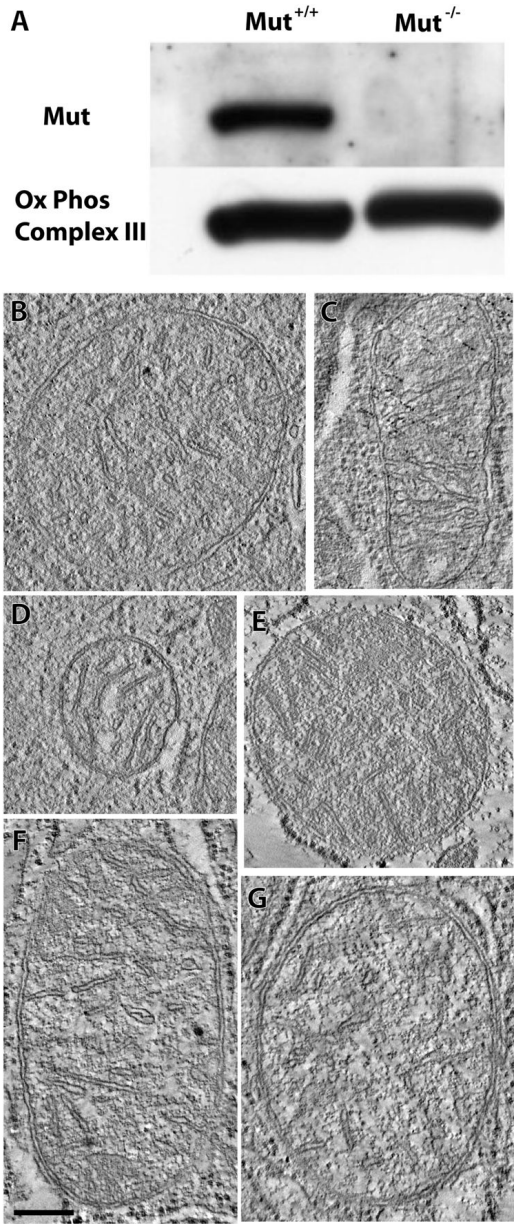

Figure 1.

A Western blot of mitochondrial mass and tomograms of individual mitochondria. (A) While mutase levels were undetectable in the *Mut* $^{-/-}$ tissue, levels of a marker of mitochondrial mass, oxidative phosphorylation complex III core II, were similar in control and *Mut* $^{-/-}$ mouse liver tissue. (B, C and D) A 2.2 nm thick tomographic slice through three different mitochondria from the control sample. (E, F and G) A 2.2 nm tomographic slice through three different mitochondria from the *Mut* $^{-/-}$ sample. The scale bar is 250 nm.

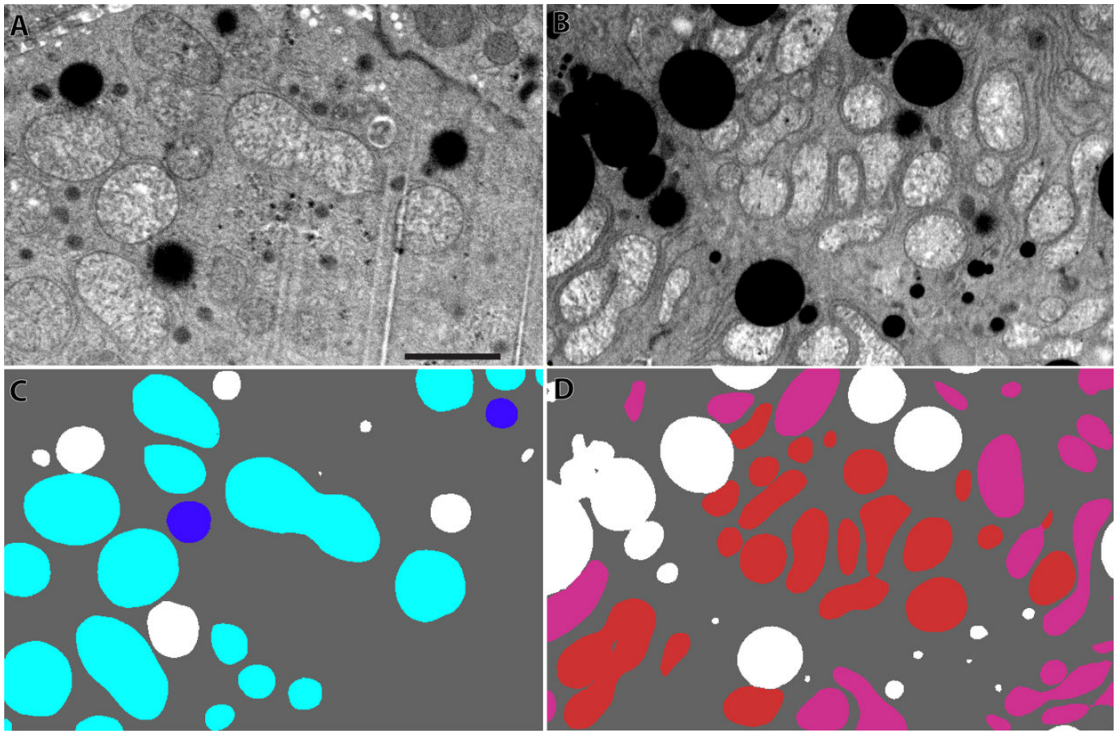

Figure 2.

Backscattered SEM images of murine liver cells. (A) A backscattered image of a portion of a control murine liver cell showing the density distribution. The dark objects are lipid bodies. (B) A backscattered image of a *Mut* $^{-/-}$ murine liver. (C) A segmentation of panel A with lipid in white, whole mitochondria in blue and partial mitochondria (those that run off the edges of the reconstructed volume) in aqua. (D) A segmentation of panel B with lipid again in white, whole mitochondria in red and partial mitochondria in pink. *Mut* $^{-/-}$ liver tissue has more and more contorted mitochondria. The scale bar is 2 μm.

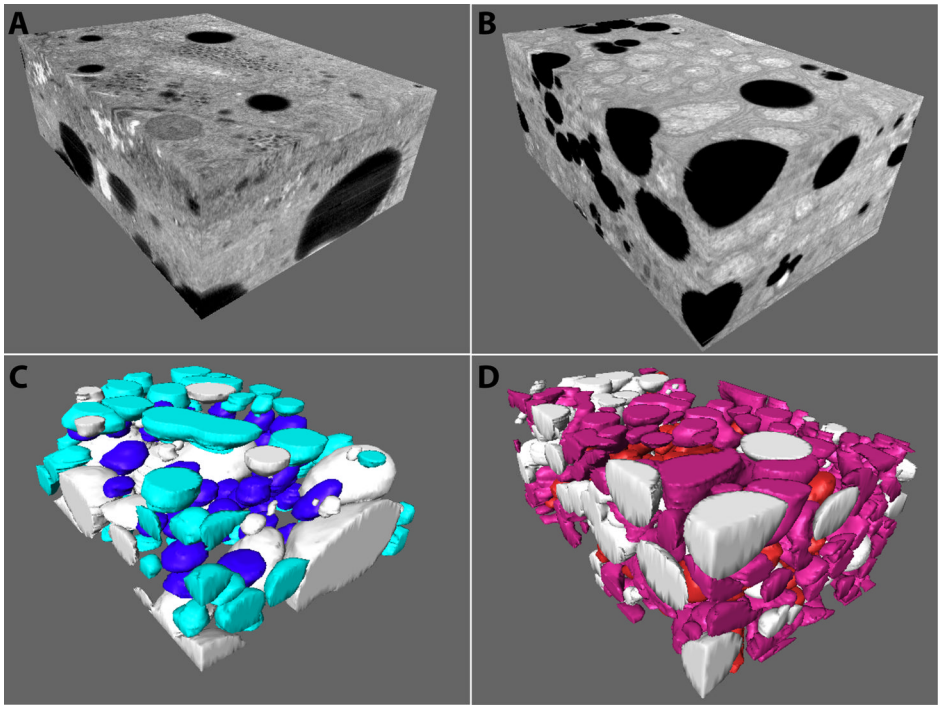

Figure 3.

3D views of the two IA–SEM reconstruction volumes of murine liver cell portions. (A) The 3D volume from a portion of the control tissue. (B) The 3D volume from the *Mut* $^{-/-}$ tissue. (C, D) Segmented representation of the control and *Mut* $^{-/-}$ tissues. Partially represented control and *Mut* $^{-/-}$ mitochondria are respectively shown in lighter colors (aqua and pink), while whole control and *Mut* $^{-/-}$ mitochondria are shown in blue and red, respectively. The volumes have dimensions of 11.3 × 8.1 × 3.9 μm (354 μm^3) and 11.8 × 7.5 × 4.9 μm (435 μm^3) for the control and *Mut* $^{-/-}$ tissues, respectively

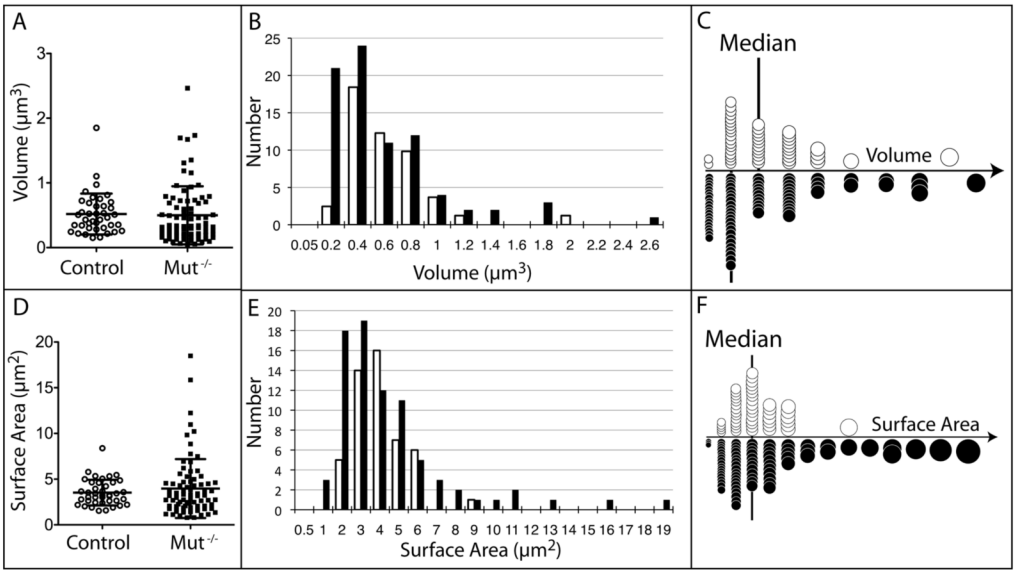

Figure 4.

Plots of the volumes and surface areas of individual, whole mitochondria. (A) Column scatter plot of volumes. Control data points are black, empty circles, while *Mut* $^{-/-}$ data points are black, filled squares. The mean and standard deviation are marked with black lines. (B) Histogram of volumes, with control values in the unfilled bar and *Mut* $^{-/-}$ values in the black, filled bars. (C) Graphic of panel B with mitochondria scaled as spheres. The median is marked with a vertical line. Unfilled circles are control mitochondrial values, while black, filled circles are *Mut* $^{-/-}$ mitochondrial values. (D) Column scatter plot of surface areas. The mean and standard deviation are marked with black lines. (E) Histogram of surface areas. (F) Graphic of panel E with mitochondria scaled as spheres. The median is marked with a vertical line.

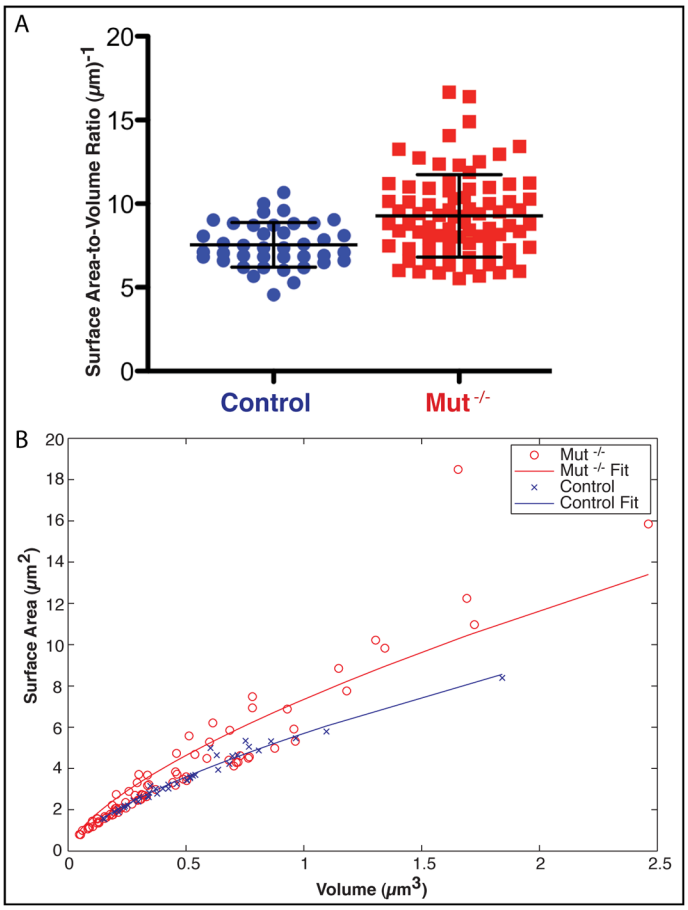

Figure 5.

Surface-area-to-volume ratios of the individual, whole mitochondria. (A) Surface-area-to-volume ratio column scatter plot, with delineated mean and standard deviation of the control and *Mut* $^{-/-}$ mitochondria. (B) Surface area plotted against volume. The lines are fit to the data, as explained in the text. Control data points are in blue, while *Mut* $^{-/-}$ data points are in red.

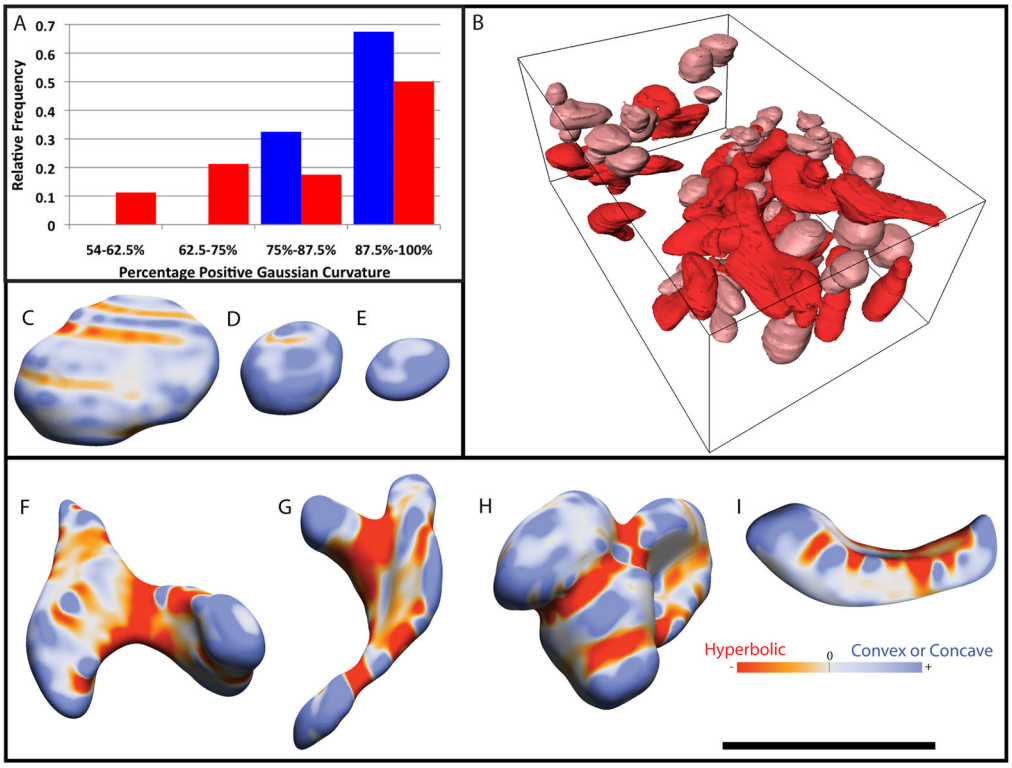

Figure 6.

Curvature of the individual, whole mitochondria. (A) Measurement of curvature displayed as a histogram of percent positive (non-hyperbolic) Gaussian curvature. Control mitochondrial values are in blue and *Mut* $^{-/-}$ mitochondrial values are in red. (B) A 3D view of all eighty, whole *Mut* $^{-/-}$ mitochondria with normal shaped mitochondria in pink and abnormal shaped mitochondria in red. (C–E) Control mitochondrial shapes. The color bar shows that red is hyperbolic Gaussian curvature and blue is either concave or convex curvature. (F–I) *Mut* $^{-/-}$ mitochondrial shapes. The black scale bar is 2 μm.

Table 1

	Mitochondrial Volume (μm^2)					Mitochondrial Surface Area (μm^2)	
	Whole Control	**Whole Mut $^{-/-}$**	**Patial Control**	**Patial Mut $^{-/-}$**		**Whole Control**	**Whole Mut $^{-/-}$**
Number of mitochondria	40	80	57	133	Number of mitochondria	40	80
Minimum	0.1515	0.05027	0.03608	0.005028	Minimum	1.54	0.79
Median	0.4466	0.3303	0.2765	0.2383	Median	3.235	3.075
Maximum	1.85	2.464	2.539	3.398	Maximum	8.39	18.49
Mean	0.5181	0.4985	0.498	04608	Mean	3.525	3.967
Standard Deviation	0.316	0.4494	0.5136	0.5239	Std Deviation	1.411	3.224
Normal distribution?	No	No	No	No	Normal Distribution?	No	No
Sum of Mito. Volumes	20.72	39.88	28.39	61.29	Sum of Mito Surface Areas	141	317.4
Comparisons of Medians					**Comparisons of Medians**		
Two-tailed Mann-Whitney Test	Whole Control vs Whole Mut $^{-/-}$		Partial Control vs Partial Mut $^{-/-}$		**Two-tailed Mann-Whitney Test**	Whole Control vs Whole Mut $^{-/-}$	
Are medians sig. different?	No		No		Are medians sig. different?	No	
P value	0.0988		0.2803		P value	0.4692	
Mann-Whitney U	1303		3415		Mann-Whitney U	1470	

Table 2

	Mitochondrial Surface Area to Volume Ratio (μm^{-1})			Percent Positive Gaussian Curvature	
	Control SA-V ratio	**Mut $^{-/-}$ SA-V ratio**		**Control**	**Mut $^{-/-}$**
Number of values	40	80	Number of values	40	80
Minimum	4.555	5.519	Minimum	77.3%	54.1%
Median	7.354	8.837	Median	91.2%	87.4%
Maximum	10.68	16.67	Maximum	100.0%	100.0%
Mean	7.54	9.273	Mean	90.7%	83.1%
Standard Deviation	1.336	2.464	Std. Deviation	66%	14.1%
Normal distribution?	Yes	No	Normal distribution?	Yes	No
Comparisons of Medians			**Comparisons of Medians**		
Two-tailed Mann-Whitney Test	Control vs Mut $^{-/-}$ SA-V ratio		**Two-tailed Mann-Whitney Test**	Control vs Mut $^{-/-}$ Curvature	
Are medians sig. different?	Yes		Are medians sig. different?	Yes	
P value	0.0002		P value	0.0203	
Mann-Whitney U	919.5		Mann-Whitney U	1183	